Drought Conditions Maximize the Impact of High-Frequency Flow Variations on Thermal Regimes and Biogeochemical Function in the Hyporheic Zone

Xuehang Song[1], Xingyuan Chen[1, *], James Stegen[1], Glenn Hammond[2], Hyun-Seob Song[1], Heng Dai[1], Emily Graham[1], and John M. Zachara[1]

[1]Pacific Northwest National Laboratory, Richland, Washington, USA.

[2]Applied Systems Analysis and Research, Sandia National Laboratories, Albuquerque, New Mexico, USA.

*Corresponding author

Email: Xingyuan.Chen@pnnl.gov; Phone: (509) 371-7510; Fax: (509) 375-2999

Key Points

- High-frequency flow variations enhance hyporheic exchange and create long-term alterations to thermal regimes and biogeochemical reactions.
- High-frequency flow variations have the largest impact on thermal regimes and biogeochemical reactions in hyporheic zone under drought.
- Spatial distribution of biogeochemical hot spots depends more on the subsurface hydraulic properties than high-frequency flow variations.

Abstract

Anthropogenic activities, especially dam operations, often induce larger and more frequent stage fluctuations than those occurring in natural rivers. However, long-term impacts of such flow variations on thermal and biogeochemical dynamics of the associated hyporheic zone (HZ) are poorly understood. In this study, we built a heterogeneous, two-dimensional, thermo-hydro-biogeochemical model for a real river system. Our results revealed important interactions between sub-daily to weekly flow variations and mean flow conditions controlled by snowpack at the watershed. High-frequency stage fluctuations had their strongest thermal and biogeochemical impacts when mean river stage was low during fall and winter. In an abnormal drought year (2015) with low river stages during summer and early fall, high-frequency stage fluctuations caused the HZ to be warmer than average. Furthermore, high-frequency stage fluctuation enhanced aerobic respiration by increasing nutrient supply while suppressing denitrification by creating more oxygenated conditions. Overall carbon consumption in the HZ increased due to high-frequency flow variations. Thermal dynamics altered by high-frequency stage fluctuation impacted biogeochemical reactions in the HZ less than effects imposed by enhanced nutrient and oxygen supply. In addition to these results, we demonstrated that the HZ's hydrogeologic properties control flow paths that influence residence times and nutrient supply, and these properties also control spatial distribution of biogeochemical reaction hot spots in the HZ. Here, we provide scientific basis for assessing potential ecological consequences of high-frequency flow variations in a regulated river, as well as guidance for maximizing potential benefits—or minimizing drawbacks—of river regulation to river ecosystems.

1. Introduction

The hyporheic zone (HZ) is a transition area where groundwater mixes with surface water and mediates the surface-subsurface exchange of water, heat, and solutes (*e.g.*, dissolved oxygen, organic carbon, carbon dioxide, nitrate, and ammonium) (*Boano et al.*, 2014; *Brunke & Gonser*, 1997). Surface-subsurface flow interactions in the HZ are critical in aquatic environments, where biogeochemical processes often are enhanced because of waters mixing from different sources

(*McClain et al.*, 2003; *Battin et al.*, 2008; *Cardenas*, 2015; *Stegen et al.*, 2016). The extent of HZ and additional bank storage, both of which can have different hydrological and/or biogeochemical definitions, are influenced by multiple complex physical features and forcing (*Boulton et al.*, 1998). These include sediment permeability and porosity (*Cardenas et al.*, 2004; *Salehin et al.*, 2004); river morphology, such as riffles, bars, and dunes (*Cardenas & Wilson*, 2007; *Buffington & Tonina*, 2009; *Stonedahl et al.*, 2013); and dynamic hydrologic boundary conditions (S*chmadel et al.*, 2016).

The dynamic hydrologic boundary condition of HZ exchange is controlled not only by natural processes (*e.g.*, snowmelt, precipitation, flood, and tidal cycles) but also by anthropogenic activities, such as dam operations. Dam construction in large river systems has been widespread in the United States (*Graf*, 1999) and across the globe (*Nilsson et al.*, 2005). Rivers regulated by dams often experience large and dynamic stage fluctuations to meet the combined demands of hydropower, irrigation, and flood control. Frequent river stage fluctuations can significantly alter the hydraulic gradient between groundwater and surface water (*Arntzen et al.*, 2006; *Fritz & Arntzen*, 2007), resulting in variations to the thermal and biogeochemical dynamics in the HZ by creating more frequent changes in gaining/losing conditions for streams or aquifers compared to steady-state flow conditions (*Sawyer et al.*, 2009; *Slater et al.*, 2010*; Francis et al.*, 2010; *Gerecht et al.*, 2011; *Ye et al.*, 2012; *Gu et al.*, 2012; *Graham et al.*, 2015; *Yellen and Boutt*, 2015; *Briody et al.*, 2016; *Trauth and Fleckenstein*, 2017). Both the thermal and biogeochemical processes in the HZ play important roles in fluvial ecology, such as benthic food production, salmonid growth, and fish spawning (*Hanrahan*, 2007; *Casas-Mulet et al.*, 2016; *Mejia et al.*, 2016). The upwelling of HZ water is especially important to temperature-sensitive organisms (*Geist et al.*, 2002; *Ebersole et al.*, 2003; *Galbraith et al.*, 2012; *Mejia et al.*, 2016).

The conceptual representation of heat transport and biogeochemical processes in the HZ of a regulated river often has been oversimplified by neglecting dynamic river stage fluctuations. Furthermore, most studies have investigated only the short-term (days to weeks) impacts of dynamic river stage fluctuations on the hyporheic temperature and biogeochemical functions, while longer-term (seasonal to inter-annual) impacts may result from the potentially long residence time of intruded river water in the associated groundwater system (*Boano et al.*, 2014). For example, the HZ's heat storage effect can persist for months (*Arrigoni et al.*, 2008; *Burkholder et al.*, 2008), and riverbed redox conditions can be impacted by seasonal hydrograph cycles (*Lautz & Fanelli*, 2008). Addressing such long-term effects of flow variations on the hyporheic thermal and biogeochemical processes requires extended observational and modeling studies with a realistic representation of hydrologic, heat transport, and biogeochemical processes within this active exchange zone.

In this paper, we address the following question: how do high-frequency flow variations, driven mainly by dam operations to meet hydropower demands, control temperature dynamics and biogeochemical fluxes in the HZ? Such understanding could provide the scientific basis needed to assess the potential ecological consequences of high-frequency flow variations caused by widespread dam operations. To address these impacts and linkages, we applied a fully coupled, two-dimensional (2D) thermo-hydro-biogeochemical model with realistically heterogeneous sediment properties along a transect perpendicular to the Columbia River. The hydrologic boundary conditions (*e.g.*, river stage and groundwater table) were progressively smoothed to remove high-frequency fluctuations. Multi-year simulations were conducted using the field-observed and smoothed hydrologic boundary conditions. The differences in their respective results of temperature dynamics, velocity, and carbon consumption in the HZ were used to assess the impacts of high-frequency flow variations. We found that high-frequency (sub-daily to weekly) flow variations had the largest impact on the hyporheic thermal regimes and biogeochemical functions when the river stage was low, whereas zones with enhanced biogeochemical activity and associated fluxes were strongly dependent on the physical heterogeneity of the alluvial layer at the top of the riverbed.

2. Methodology

2.1 Site description

The study area is situated on the western shore of the Columbia River's Hanford Reach in the 300 Area of the U.S. Department of Energy's Hanford Site, located within the semi-arid Pasco Basin in southeastern Washington State (Figure 1a). The Hanford Reach is an 80-km free-flowing section of the Columbia River with a hydroelectric dam (Priest Rapids) at its upstream boundary and impounded water (from McNary Dam) at its downstream boundary (*Duncan et al.*, 2007). As a typical regulated river, the river stage at the study site fluctuates ~0.5 meters daily and up to 2-3 meters annually. The temperature of river water varies between 5 and 22°C on an annual basis, while the temperature of groundwater remains relatively stable at ~17°C. The unconfined aquifer that exists within the river corridor and extends beneath the riverbed can be delineated into three distinct geologic formations as shown in Figure 1b: low-permeability sandy alluvium of recent fluvial deposits; high-permeability Hanford formation, consisting of coarse gravelly sand and sandy gravel; and low-permeability Ringold Formation composed primarily of silt and fine sand. More descriptions about the site hydrogeology can be found in previous studies by *Bjornstad et al.* (2009), *Chen et al.* (2012; 2013), and *Zachara et al.* (2013; 2016).

2.2 Spectral decomposition of river discharge and river stage

High-frequency variations (sub-daily to weekly) in the river stage are driven by dam operations upstream from the study site. A wavelet-based spectral analysis method was applied to determine dominant frequencies of variations in the time series of: 1) the observed hourly river stage in our site and 2) the observed and naturalized daily river discharges below the Priest Rapids Dam. These discharge data were obtained from the River Management Joint Operating Committee (http://www.bpa.gov/power/streamflow/default.aspx). The naturalized river discharge here denotes the flow scenario with no dam operations. The observed and naturalized river discharges were used as surrogates of river stage to identify the signature frequencies unique to dam operations because the river discharge is the ultimate driver of the river stage variation, while there is no naturalized river stage for the system. The spectral decompositions performed on the observed river discharge and river stage, shown in Section 3.1, confirmed that these two time series share the same set of dominant frequencies, except for the sub-daily frequency stemming from the resolution of the river discharge data.

We used an R package, "WaveletComp" (*Roesch & Schmidbauer*, 2015), for the spectral analysis, wherein the wavelet transform of a time series is defined as the convolution of the series with a set of "wavelets daughters" as follows:

$$\mathrm{Wave}(\tau, s) = \sum_t x_t \frac{1}{\sqrt{s}} \psi_0^* \left(\frac{t-\tau}{s} \right), \tag{1}$$

where x_t denotes the data point at time t of the time series to be decomposed (*e.g.*, the discharge and stage data in this study) and * denotes the complex conjugate, the scaling parameter s

determines the daughter wavelet's coverage in the frequency domain, and the localizing time parameter τ determines the daughter wavelet's location in the time domain. ψ_0 is the Morlet "mother" wavelet defined as:

$$\psi_0(t) = \pi^{-1/4} e^{i\omega t} e^{-t^2/2}, \tag{2}$$

where the dimensionless frequency ω is set as 6 to ensure that the Morlet function has zero mean and is localized in both time and frequency space (*Farge*, 1992). The wavelet power spectrum describes the time-frequency wavelet energy density as:

$$\mathrm{Power}(\tau, s) = \frac{1}{s} \left| \mathrm{Wave}(\tau, s) \right|^2 \ . \tag{3}$$

To measure the relative contribution of the variation at a given frequency to the total variation, a time-averaged wavelet power at a given scale parameter s can be calculated from Eq. (3). The higher the time-averaged wavelet power, the more significant the frequency is in the entire spectrum window.

After the dominant frequencies of flow variations were identified, we applied moving average as a low-pass filter to remove frequencies higher than the moving window in the river stage and inland groundwater table to drive model simulations under less dynamic flow conditions. The model simulation using the original, highly dynamic hydrologic boundary conditions without filtering was engaged as the baseline case to assess the change in the hyporheic exchange fluxes and associated biogeochemical processes caused by the dam-induced high-frequency flow variations.

2.3 Numerical model configuration

To simulate lateral and vertical HZ exchange, we constructed a 2D bank storage model with the river and groundwater aquifer as two end members of the river corridor system. The model domain was 143.2 m in the horizontal direction and 20 m in the vertical. The model's geological structure was informed by previous geological and geophysical surveys (*Williams et al.*, 2008; *Chen et al.*, 2013). The hydraulic and thermal properties were modified from earlier modeling studies performed at the same site (*Ma et al.*, 2012; *Chen et al.*, 2013) (Table 1). Heterogeneous permeability fields of the alluvium and Hanford formation (Figure 1b) were generated with unconditional geostatistical simulations via the R package "gstat" (*Pebesma*, 2004) using the exponential variogram model with the parameters shown in Table 1. The grid size was refined near the shoreline (a rectangle covering the entire alluvium and its surrounding Hanford and Ringold formation sediments with cells measured at 0.1 m in the horizontal and 0.05 m in the vertical) to capture the fine details of exchange dynamics in the HZ. To avoid numerical instability, the grid sizes for the rest of the domain were progressively increased by 9%. The total number of grid cells was nearly 0.2 million.

2.3.1 Biogeochemical function

The biogeochemical functions in the HZ are regulated by microbial activities. Microbes control enzyme levels and activities for the preferential use of electron donors and acceptors that optimally promote their growth. In lieu of empirical inhibition kinetics (*e.g., Gu et al.,* 2007; *Trauth et al.*, 2014), we adopted the cybernetic modeling approach developed by *Ramkrishna and Song* (2012) to account for the microbial regulation. The cybernetic approach views organisms as teleonomic systems that regulate metabolism to promote a certain metabolic objective in a varying environment, where analytic forms of regulation rules (called "cybernetic control laws") can be derived using an optimal control theory (*Kompala et al.*, 1986; *Young & Ramkrishna*, 2007). The effectiveness of the cybernetic modeling was successfully demonstrated in previous case studies of modeling denitrifying organisms (*Song & Liu*, 2015) and microbial communities (*Song et al.*, 2014). In the present work, we used a simplified version of the cybernetic model developed by *Song et al.* (2017) for linking microbial communities with enzyme expression observed in a denitrification experiment (*Li et al.,* 2017). The Supplementary Material provides more details related to the derivation of the simplified cybernetic model (Text S1).

A two-step denitrification and oxidative respiration were considered in our HZ biogeochemical reaction network based on laboratory batch experiments (*Li et al.*, 2017):

$$\begin{aligned} &CH_2O \;+\; 2NO_3^- \rightarrow 2NO_2^- + CO_2 + \; H_2O \\ &CH_2O \;+ 4/3NO_2^- + \; 4/3H^+ \rightarrow 2/3N_2 + CO_2 + \; 5/3H_2O \, . \\ &CH_2O \;+\; O_2 \rightarrow CO_2 + \; H_2O \end{aligned} \tag{4}$$

In Eq. (4), multi-stage reduction from NO_2^- to N_2 is lumped into a single reaction by assuming relatively fast dynamics of nitrogen oxide intermediates, such as NO and N_2O.

Microbial biomass ($C_5H_7O_2N$) synthesis was considered as:

$$CH_2O \ + \ 1/5NH_4^+ \rightarrow 1/5C_5H_7O_2N + \ 3/5H_2O \ + \ 1/5H^+ . \qquad (5)$$

Depending on what electron acceptors are available in the environment, microbes obtain energy for growth and maintenance through aerobic or anaerobic respiration. To account for this coupling, each of the energy-producing reactions in Eq. (4) is combined with biomass synthesis reaction in Eq. (5) as follows:

$$\begin{aligned} &CH_2O + 2f_1NO_3^- + \frac{1}{5}(1-f_1)NH_4^+ \rightarrow 2f_1NO_2^- + f_1CO_2 + \frac{1}{5}(1-f_1)C_5H_7O_2N \\ &CH_2O + 2f_2NO_2^- + \frac{1}{5}(1-f_2)NH_4^+ \rightarrow \frac{2}{3}f_2N_2 + f_2CO_2 + \frac{1}{5}(1-f_2)C_5H_7O_2N \ , \\ &CH_2O + f_3O_2 + \frac{1}{5}(1-f_3)NH_4^+ \rightarrow f_3CO_2 + \frac{1}{5}(1-f_3)C_5H_7O_2N \end{aligned} \qquad (6)$$

where f_1, f_2, and f_3 are parameters denoting the fractional contribution of energy-producing pathways in Eq. (4). With sole focus on simulating carbon and nitrogen cycling, H^+ and H_2O are omitted in the equations above. Reactions in Eq. (6) share the same electron donor (CH_2O) but involve different electron acceptors (*i.e.*, NO_3^- and NO_2^- for anaerobic respiration; O_2 for aerobic respiration), thus representing three alternative pathways for biomass production ($C_5H_7O_2N$). The reactants and products in the simulations include $C_5H_7O_2N$, CO_2, CH_2O, O_2, NO_3^-, NO_2^-, and N_2. Hereafter, for simplicity we use *DOC* (dissolved organic carbon), *DIC* (dissolved inorganic carbon), and *BM* (biomass) to denote CH_2O, CO_2, and $C_5H_7O_2N$, respectively.

Dynamic mass balances of key variables in simulation can be written based on the stoichiometric equation, *i.e.*, Eq. (6), as follows:

$$\frac{d}{dt}\begin{bmatrix}[DOC]\\ [O_2]\\ [NO_3^-]\\ [NO_2^-]\\ [N_2]\\ [DIC]\\ [BM]\end{bmatrix}=\begin{bmatrix}-1 & -1 & -1\\ 0 & 0 & -f_3\\ -2f_1 & 0 & 0\\ 2f_1 & -4f_2/3 & 0\\ 0 & 3f_2/2 & 0\\ f_1 & f_2 & f_3\\ (1-f_1)/5 & (1-f_2)/5 & (1-f_3)/5\end{bmatrix}\begin{bmatrix}r_1\\ r_2\\ r_3\end{bmatrix}[BM]\ , \qquad (7)$$

where r_1, r_2, and r_3 are the regulated reactions rates for aerobic respiration and denitrification (described later). By assuming a fixed biomass degradation rate k_{deg} [1/d], we derived the following partial differential equations for DOC and BM:

$$\frac{d[DOC]}{dt}=-\left(r_1+r_2+r_3-5k_{\text{deg}}\right)[BM]\ , \qquad (8)$$

$$\frac{d[BM]}{dt}=\left(\frac{1-f_1}{5}r_1+\frac{1-f_2}{5}r_2+\frac{1-f_3}{5}r_3-k_{\text{deg}}\right)[BM]\ . \qquad (9)$$

Reaction rates for the oxidative respiration and two-step denitrification in Eqs. (7-9) were modeled as being catalyzed by distinct enzymes:

$$r_i=e_i^{rel}r_i^{kin}\ ,i=1,2,3\ , \qquad (10)$$

where i is the generic reaction index; e_i^{rel} 's denote the relative level of enzymes that catalyze the two-step denitrification reactions and aerobic respiration, respectively; and r_i^{kin} 's are unregulated reaction rates that can be represented by the Monod kinetics, *i.e.*,

$$r_i^{kin}=k_i\frac{d_i}{K_{d,i}+d_i}\frac{a_i}{K_{a,i}+a_i},\quad i=1,2,3, \qquad (11)$$

where k_i is the maximum specific uptake rate of organic carbon (CH_2O) (mol $L^{-1}d^{-1}$), a_i is the electron acceptor concentration (mol L^{-1}), d_i is the electron donor concentration (mol L^{-1}), $K_{a,i}$ is the half-saturation constant for electron acceptors (mol L^{-1}), and $K_{d,i}$ is the half-saturation constant for electron donors (mol L^{-1}). The enzyme levels are determined through a direct linkage to the cybernetic control laws (*Young & Ramkrishna*, 2007) (Text S1), *i.e.*,

$$e_i^{rel} = \frac{r_i^{kin}}{\sum_{j=1}^{3} r_j^{kin}},\ i = 1,2,3 \quad (12)$$

,

which implies that microbes control the synthesis of enzymes in proportion to their relative contribution to a given objective (*e.g.*, the carbon uptake rate). This formulation enables the simulation of dynamic shifts among all three electron acceptors (*i.e.*, O_2, NO_3^-, and NO_2^-)—without empirical inhibitive kinetics.

We also considered the effect of temperature on reaction rate using the Arrhenius equation:

$$r_i = A_i e^{\frac{-E_a}{RT}},\ i = 1,2,3\ , \quad (13)$$

where r_i is the reaction rate under temperature T (in Kelvin) with subscript i being the generic reaction index, E_a is the activation energy (0.65 ev in this study), R is the gas constant (8.314 J mol^{-1} K^{-1}), and A_i is the pre-exponential factor. We derived the base reaction rate for each reaction from laboratory batch experiments under the room temperature of 26ºC. The reaction rates under other temperatures were scaled from the base rates, $r_{base,i}$, as follows,

$$r_i = r_{base,i} \exp\left[-\frac{E_a}{R}\left(\frac{1}{T} - \frac{1}{26+273.15}\right)\right],\ i = 1,2,3\ . \quad (14)$$

In all of the simulations, key parameters of denitrification, including f_1, f_2, k_1, k_2 and k_{deg}, were estimated from the batch denitrification data collected by *Li et al.* (2017). Literature values were used for the half-saturation constants associated with DIC for electron donors (*i.e.*, k_{d1} and k_{d2}) and electron acceptors (*i.e.*, k_{a1} and k_{a2}) (*Yan S. et al.*, 2016; *Rittmann & McCarty* 2001). Parameters associated with oxidative respiration are determined by assuming: 1) oxidative respiration is energetically more favorable than NO_3- reduction (*i.e.*, f_3=f_1/3; k_3=3k_1), and 2) half-saturation constants are the same for different reactions (*i.e.*, $K_{a,3}$= $K_{a,1}$; $K_{d,3}$= $K_{d,1}$). This parameter setting leads to the sequential utilization of three alternative electron acceptors, *i.e.*, O_2, NO_3-, NO_2- in batch reactor simulation (Text S2 and Figure S1). Table 2 provides a summary of the model parameters used in the simulations.

2.3.2 Simulator and boundary conditions

The massively parallel subsurface flow and reactive transport code PFLOTRAN (pflotran.org) (*Hammond et al.*, 2014) was used to simulate coupled thermal-hydro-biogeochemical processes. The governing flow equation in PFLOTRAN is the Richards equation with Darcy's law, which is fully coupled with the energy conservation equation for heat transport. The solute transport mechanisms include advection and macrodispersion, while molecular diffusion is neglected because of its small contribution compared to the macrodispersion in the presence of heterogeneity in the permeability field. We customized the reaction network described in Section 2.3.1 using reaction sandbox in PFLOTRAN. Simulations were performed for a six-year time window (2010-2015). The first year was used for model spin-up, while the other five years were used for analysis.

A transient hydrostatic hydraulic head and a Dirichlet temperature boundary condition were used at both the river and inland boundaries. A seepage face was applied at the river bank exposed to the atmosphere. Water level and temperature data were taken from a nearby gauge in the Columbia River and the inland groundwater monitoring well (shown in Figure 1a). The top and bottom boundaries were set as no-flow and no-heat transfer as surface recharge is small in the semi-arid climate zone (*Rockhold et al.*, 1995), while the bottom of the modeling domain was constrained by the fine-grained Ringold Formation that serves as a local aquitard.

The solute boundary conditions were based on field sampling results. Both the river water and groundwater are rich in dissolved oxygen (~100% for river water and ~80% for groundwater). The solute concentrations of CH_2O, HCO_3^-, and NO_3-, provided in Table 3, were taken from averaged field sampling results (*Zachara et al*., 2012; 2016). DOC in the river water was assumed to be the main carbon source, *i.e.*, CH_2O, for the biogeochemical processes in the HZ, while groundwater was the main source for NO_3^-. The high dissolved oxygen and low DOC concentrations in groundwater implied that aerobic respiration was the dominant HZ biogeochemical process at the site (*Stegen et al.*, 2016).

2.3.3 Simulation scenarios

Different simulation scenarios were constructed to investigate the impacts of the high-frequency flow variations induced by dam operations on hyporheic exchange fluxes and biogeochemical functions using either the original or smoothed river stages and inland groundwater table as the flow boundary conditions. The case with original flow boundary conditions served as the baseline case (Case 1) . Based on the wavelet-based spectral analysis results, the weekly smoothed case was chosen to represent the scenarios without high-frequency dam operations (Case 2). The differences between the two cases in simulated hyporheic exchange, thermal regime, and associated biogeochemical processes between cases are analyzed in the following sections to examine the effects of dam-induced high-frequency flow variations on hyporheic processes.

3. Results and Discussion

3.1 River discharge and stage spectral analyses results

Real observed and naturalized discharges at the Priest Rapids Dam (Figure 2a) showed vastly distinct peak flows and seasonal patterns over the course of a year. However, their spectral analyses (Figure 2b) revealed the dominance of semi-annual and annual cycles in both time series, represented by the peaks of the time-averaged wavelet powers. The wavelet power peaks at sub-weekly frequencies were only present in the observed discharge, not in the naturalized discharge, indicating that sub-weekly frequency variations are caused by dam operations.

The real observed hourly river stage and groundwater table in the inland wells showed robust annual cycles (Figure 3a). The groundwater temperature was relatively stable compared to the river temperature (Figure 3b). All observations resulted from long-term monitoring efforts at hourly frequency. Data gaps within a few hours were filled with moving averages of neighboring points. The spectral analysis on the original hourly river stage data (Figure 3d, blue line) showed a visible peak at the daily frequency, a weak peak at the weekly frequency, and two dominant peaks at the semi-annual and annual frequencies, which is consistent with the characteristic frequencies of the observed discharge data. Moving averages using window sizes of one day and one week then were applied to the observed river stage data to remove the two signature frequencies of flow variations induced by the dam operations. Figure 3c shows the smoothed river stages with these two different averaging windows along with the original data from a two-month period in 2013. The smoothing effects of moving average are evident in the time series plot, and the removal/filtering of the targeted frequencies was confirmed in the spectral analyses results performed on these two smoothed hydrographs (Figure 3d, dashed lines). The same moving average procedure was applied to the inland groundwater table data to generate consistent hydrologic boundary conditions at the both ends of the model domain.

3.2 Effects of high-frequency flow variations on thermal regime

The simulations revealed a cold zone in the middle of the alluvium in summer (Figure 4a, Case 1), which was ~5ºC colder than the adjacent inland groundwater and river water. To better illustrate the long-term thermal dynamics in various depths of the HZ, we took two, one-dimensional (1D) vertical columns from the 2D model domain (the black vertical lines marked in Figure 4a) and generated heat maps of their temperature profile over time (shown in Figure 4b-c). These heat maps exhibited the temporal dynamics (x axis) of the temperature in selected vertical columns (y axis). The first vertical column C1 originated in the riverbed at an elevation roughly in the middle of the river stage fluctuation zone, while the second vertical column C2 originated at an elevation in the lower end of this fluctuation zone. We overlaid river stage time series and depths of the Hanford and Ringold formations on the heat maps to inspect the interactions between the spatio-temporal thermal dynamics and river stage dynamics. As evident in Figure 4b-c, the intrusion of cold river water in winter and early spring gradually cooled the shallow alluvium. This cold zone moved deeper into the riverbed with the intrusion flow until the temperature in the shallow HZ started to increase again in the following summer. The propagation of the warm zone followed a similar pattern with that of the cold zone. Although the size of this cold zone varies over the years and with the soil column location, it could persist in the HZ for nearly half a year, which is demonstrated in Figure 4. This phenomenon is consistent with field observations that discovered persistent (for months) heat storage in the HZ (*Arrigoni et al.*, 2008; *Burkholder et al.*, 2008).

The existence of the cold zone also was revealed by a multi-depth thermistor array installed at the study site in spring 2016, which measures the river and HZ temperatures at depths of 4 cm, 24 cm, and 64 cm below the riverbed, respectively. Figure 5 shows the temperature data from the array, from which cooler temperatures (~4-5ºC lower) than both the river water and groundwater were observed at 24 cm and 64 cm below the riverbed in June and July. This cool temperature was close to the river water temperature in April, indicating a long residence time of river water in the groundwater system (*McCallum & Shanafield*, 2016) and/or heat storage effect of the aquifer sediments (*Constantz*, 2008).

The presence and persistence of cold zones also were yielded in the simulations driven by the daily and weekly smoothed hydrologic boundary conditions. The differences in temperature fields between the baseline case (Case 1) and the smoothed cases represent the effects of high-frequency flow variations on the HZ thermal regime. There were negligible differences between the daily and weekly smoothed cases, indicating that most of the variances were caused by daily to sub-daily variations. Therefore, we based our analyses of high-frequency stage fluctuation impacts on the differences between the cases with original hourly boundary condition (Case 1) and those with weekly smoothed boundary condition (Case 2).

Under the high-frequency river fluctuations, the shallow HZ in column C1 could be ~10ºC colder in winter and early spring (blue areas in Figure 6a) and ~5ºC warmer in summer and early fall 2015 (red areas in Figure 6a). These results were revealed by examining the temperature difference between cases with original hourly boundary condition (Case 1) and weekly smoothed boundary condition (Case 2), and they implied enhanced heat exchanges between the river and the HZ. The maximum difference of temperature along column C1 was capped at 2ºC to further show the fine details of temperature difference (Figure 6b). Similar temperature difference patterns were generated along column C2 (Figure 6c), which is located deeper in the riverbed. However, the magnitude of temperature difference was much smaller along column C2 because the high-frequency stage fluctuations cause the most significant differences in areas that would stay dry without those fluctuations.

Figures 6b and 6c also show that the more significant temperature differences caused by the high-frequency river stage fluctuations resulted during the lower river stage period, which usually occur during late fall and early winter. The high-frequency river stage fluctuations could have induced more frequent changes in flow directions, which would otherwise be dominated by unidirectional outflow during lower river stages. Consequently, the exchange of mass and heat between the river and groundwater systems were enhanced by this more frequent change in flow directions. On the contrary, the high-frequency flow variations had little effect on the hyporheic exchange during higher river stages because they could hardly change the dominant inflow direction or magnitude. To further investigate the linkage between river stage and hyporheic exchange increased by high-frequency flow variations, we retrieved the exchange flux time series across the riverbed for Case 1 and Case 2 then compared the percentage difference of these two exchange fluxes as a function of river stage in Figure 7. The percentage difference of exchange flux p_{Flux} is calculated by

$$p_{Flux} = \frac{F_1 - F_2}{F_2} \times 100\% , \tag{15}$$

where F_1 [m^2/s] and F_2 [m^2/s] are the exchange fluxes of Case 1 and Case 2, respectively. We used p_{Flux} to represent the net contribution of high-frequency flow variation to exchange flux (both in and out). Figure 7 demonstrates that the p_{Flux} could be quite large (up to 400%) when river stage was low. The total exchange flux across the river boundary of the baseline case (Case 1) was 68% higher than the weekly smoothed case (Case 2). Taking the mean river stage (105.5 m) during the five-year simulation as a threshold, the total exchange fluxes of Case 1 were significantly larger (207%) than those of Case 2 when river stages were lower than 105.5 m. Meanwhile, their difference was relatively small (34%) when river stages exceeded 105.5 m.

The high-frequency flow variations enhanced the intrusion of cold river water in winter generating cooler HZ, while they led to warmer HZ temperatures during late summer when the river stage was low and the river water temperature was still warm. Significantly warmer HZ temperatures resulted in the summer and fall of 2015 because of extreme drought conditions caused by the thin snowpack in the headwater catchments (*Anderson et al.*, 2016). On average, the high-frequency flow variations lowered the hyporheic temperature by 0.13ºC over the five-year time window of our simulation. As the benthic temperature impacts fish spawning and growth (*Mejia et al.*, 2016), the stronger impact of high-frequency flow variations on the HZ thermal regime under low flow conditions has significant ecological implications with respect to dam operations. For example, dam operations in winter could cool down sediments and store cold water to buffer the temperature increase in summer, creating thermal refugia for coldwater fish species (*Caissie*, 2006; *Kurylyk et al.*, 2015; *Whitledge et al.*, 2006). However, dam operations during drought years should enact plans to minimize the potential adverse ecological consequences.

3.3 Effects of high-frequency flow variations on biogeochemical reactions

As each reaction consumed organic carbon, the carbon consumption rate and cumulative carbon consumption were adopted as key criteria in this study to identify the biogeochemical reaction hot spots, quantify contributions of each reaction, and assess the impacts of high-frequency flow variations on HZ biogeochemical activities.

The spatial distributions of cumulative carbon consumption in all three individual reactions from Case 1 (shown in Figure 8) exhibited similar spatial structure. The oxidative respiration (Figure 8b) accounted for most of the total consumption (92.7%) because both the groundwater and river water were well oxygenated. The results also indicated the dependence of biogeochemical processes on flow and transport processes as: 1) the near-shore alluvial layer was the most biogeochemically active domain, which was consistent with the results obtained by *Gu et al.* (2012) assuming homogenous permeability; and 2) the spatial distribution of biogeochemically active zones was similar to that of the mean velocity field during the simulation window (Figure 9). Figure 10 illustrates the relation between the cumulative carbon consumption in alluvium and mean velocity and permeability field. These scatter density plots confirmed the strong dependence of total carbon consumption on the HZ's hydrogeologic properties, which consequently controls the flow paths that influence residence times and nutrient supply.

By comparing the total carbon consumption of the baseline case (Case 1) and the weekly smoothed case (Case 2), it showed carbon consumption increased by 19.1% across the entire domain with 18.0% increase in alluvium and 64.9% increase in the Hanford formation due to the enhanced hyporheic exchange under high-frequency flow variations. The percentage of increase in Hanford formation appears more significant due to its relative small amount of total carbon consumption. The overall structure of biogeochemically active zones of the weekly smoothed case (Figure 11) was similar to the baseline case (Figure 8) because the river intrusion followed similar paths in the two cases under the assumption of river water being the main carbon source.

More details regarding the influence of high-frequency fluctuations on spatial distribution of carbon consumption appear in Figure 12, which plots the percentage difference of the cumulative carbon consumption of Case 1 to Case 2. The percentage differences of total and individual cumulative carbon consumption p_{Cumu} were calculated by

$$p_{Cumu,i} = \frac{C_{i,1} - C_{i,2}}{C_{i,2}} \times 100\%, \; i = 1,2,3 \;, \qquad (16)$$

where $C_{i,1}$ [mol/m^2] and $C_{i,2}$ [mol/m^2] are the cumulative carbon consumptions in the *i*th reaction for Case 1 and Case 2, respectively. We used $p_{Cumu,i}$ to represent the net contribution of high-frequency flow variations to carbon consumption. Our notable observations include: 1) the high-frequency fluctuation increased the carbon consumption in all the reactions right below the riverbed because of the increased supply of all reactants associated with higher mass exchange, 2) the oxidative respiration increased in alluvium along the preferential flow path because of the increased carbon and oxygen supply by high-frequency fluctuation (Figure 12a), and 3) the denitrification in alluvium was slightly suppressed by the high-frequency fluctuations (Figure 12c,d) because the increased oxygen concentration and the enhanced oxidative respiration left less DOC available to the denitrification process, and 4) the high-frequency fluctuations increased the carbon consumption in all reactions in the Hanford formation because it increased carbon supply into the deeper zone (Figure 12a-d).

The impact of high-frequency flow variations on carbon consumption also was maximized during low river stage periods as shown in the scatter density plots of the percentage difference of carbon consumption rate in alluvium in Case 1 to Case 2 versus river stage (Figure 13a). Similar to the cumulative carbon consumption rate, the percentage difference of carbon consumption rate was calculated by

$$p_{Rate,i} = \frac{r_{i,1} - r_{i,2}}{r_{i.2}} \times 100\%,\ i = 1, 2, 3\ , \tag{17}$$

where $r_{i,1}$ [mol/(m^{2}s)] and $r_{i,2}$ [mol/(m^{2}s)] are the carbon consumption rates by the *i*th reaction for Case 1 and Case 2, respectively. The oxidative respiration was mostly enhanced by the high-frequency flow variations during low river stage periods (Figure 13b), while the denitrification was generally decreased because of the inhibition imposed by more oxygenated condition and increased DOC consumption by the oxidative respiration at the same time (Figure 13c-d).

The enhanced hyporheic biogeochemical processes driven by the high-frequency flow variations could have attendant effects on riverine benthic food webs (*Baxter et al.*, 2005; *Richardson et al.*, 2010), fish spawning (*Mejia et al.*, 2016), and organic contaminant biodegradation (*Conant et al.*, 2004). These biogeochemical effects may be compounded at the low river stage when the HZ temperature also is highly impacted by the high-frequency flow variations.

3.4 Quantifying the impacts of high-frequency flow variations on biogeochemical processes contributed from the transport process and thermal effects

High-frequency flow variation affects HZ biogeochemical activities in two ways: enhanced nutrient and oxygen supplies and altered HZ temperature. It is difficult to separate the individual contributions from each of the effects because the kinetic reaction rates at a given location are regulated by reactant concentrations that are a result of both effects before the arrival at the given location. As an approximation, we decomposed the kinetic temperature-dependent reaction rates based on Eq. (14) into their base rates and temperature-dependent scaling factors for the two simulation cases as:

$$
\begin{aligned}
r_{i,1} &= r_{base,i,1}\exp\left[-\frac{E_a}{R}\left(\frac{1}{T_1}-\frac{1}{299.15}\right)\right],\ i=1,2,3 \\
r_{i,2} &= r_{base,i,2}\exp\left[-\frac{E_a}{R}\left(\frac{1}{T_2}-\frac{1}{299.15}\right)\right],\ i=1,2,3
\end{aligned}
. \qquad (18)
$$

The ratio between the reaction rate for the two cases is then a product of a ratio between their base rates ($C_{S,i}$) and a ratio between their temperature scaling factors (C_T) as:

$$
\begin{aligned}
\frac{r_{i,1}}{r_{i,2}} &= C_{S,i}\cdot C_T,\ i=1,2,3 \\
C_{S,i} &= \frac{r_{base,i,1}}{r_{base,i,2}},\ i=1,2,3 \\
C_T &= \exp\left[-\frac{E_a}{R}\left(\frac{1}{T_1}-\frac{1}{T_2}\right)\right]
\end{aligned}
. \qquad (19)
$$

The ratio between the temperature scaling factors in these two cases do not vary among different reactions because we used the same activation energy for all reactions. $C_{S,i}$ and C_T represent the impacts on reaction rates in Case1 and Case2 caused by reactant concentration and temperature dependence, respectively. The cumulative effects of these two factors on the total carbon consumption rates from all reactions in the two cases are then quantified as:

$$
\begin{aligned}
P_C &= \left(\frac{\sum_{i=1}^{3} r_{i,1}}{\sum_{i=1}^{3} r_{i,2}}-1\right)\times 100\% \\
P_S &= \left(\frac{\sum_{i=1}^{3} r_{i,1}}{\sum_{i=1}^{3} r_{i,2}C_T}-1\right)\times 100\%, \\
P_T &= \left(C_T-1\right)\times 100\%
\end{aligned}
\qquad (20)
$$

where P_C is the percentage difference of carbon consumption rate for all the three reactions induced by high-frequency flow variation, representing the combined effects from solute transport and temperature dependence of reaction rates; P_S is the percentage difference of carbon consumption rate for all the three reactions contributed by altered solute transport, and P_T is the percentage difference of carbon consumption rate for all the three reactions contributed by altered temperature.

Our results show that the altered HZ temperature by induced by high-frequency fluctuation had relatively small impact on reaction rates, accounting for about 1.4% decrease across the entire domain with 1.3% decrease in the alluvium and 1.7% decrease in the Hanford formation. The percentage of decrease in Hanford formation appears is slightly bigger due to its relatively small reaction rates. The small decrease of reactions rate is consistent with the small change in the average temperature in the HZ (0.13ºC decrease as mentioned in Section 3.2) induced by the high-frequency river stage fluctuations in the five-year simulation. The temperature contribution to biogeochemical reactions from the high-frequency flow variation appears more significant around the preferential flow path within the fluctuation zone, as demonstrated by the time-averaged P_T in Figure 14. In general, the reaction rates are decreased by the high-frequency flow variations because of more cold water intrusion in the HZ, with the only exception found around the right bottom of the model domain where higher temperature was resulted from the high-frequency flow variation. A potential cause of the abnormal phenomenon is the low flow velocity close to the no-flow boundary, leading to dominance of thermal conduction over mass exchange on the temperature variation.

4. Summary and Conclusion

High-frequency flow variations are a common phenomenon in most regulated river systems, which experience more abrupt and frequent fluctuations than natural rivers. As identified using the river stage and dam discharge data from the Hanford Reach of the Columbia River via wavelet spectrum analysis techniques, dam operations induced robust short-term (daily to weekly) river stage fluctuations due to regional electric demand. It has been previously reported that river regulation by dam operation can enhance hydrologic exchange within and through the HZ, but the attendant effects on the long-term thermal regime and biogeochemical processes of the HZ have not been established. Here, we provided an initial assessment of these significant effects using a newly developed thermal-hydro-biogeochemical model with lab-calibrated reaction rates for and supported by field monitoring data.

Through the numerical simulation, we revealed a long-term persistent cold-water zone in the riverbed after winter, which also was verified by observational data from a multi-depth thermistor array. High-frequency flow variations enhanced the heat exchange between the river and HZ, and the maximum temperature difference within the HZ could reach up to 5~10ºC. The high-frequency flow variations also created long-term alterations to thermal regimes in the HZ and reduced average HZ temperature by 0.13ºC.

Biogeochemical reactions in the HZ, as represented by the DOC consumption, were significantly enhanced by the high-frequency flow variations, mainly due to enhanced mass exchange while the altered HZ temperature had minor effects through temperature-dependent reaction rates. After considering daily and weekly stage fluctuations induced by dam operations, the total carbon consumption was increased by 19.10%, with 1.4% decrease contributed by the altered HZ temperature. The spatial distribution of biogeochemical hot spots, on the other hand, highly depends on subsurface hydraulic properties rather than influenced by the high-frequency flow variation.

The mean river stage is one of the most important control factors in considering the impact of high-frequency flow variations on both the thermal regime and biogeochemical dynamics in the HZ. Compared to high river stage periods, the high-frequency fluctuations during low river stages, especially when under drought conditions, can induce more frequent changes in flow directions rather than being unidirectional outflow, thus creating more water, thermal and biogeochemical exchanges.

The thermal and biogeochemical dynamics in the HZ are important to fluvial ecology, such as thermal refugia for fish spawning and growth, benthic food production, and nitrate removal. As a regulated system, the Hanford Reach of the Columbia River is not unique in experiencing strong daily and weekly rhythms driven by hydropower demands that shift the thermal and biogeochemical regimes in the HZ. This study has provided the scientific basis to assess the potential ecological consequences of the high-frequency flow variations in a regulated river, as well as guidance on how to maximize the potential benefits, or minimize the drawbacks, of river regulation to river ecosystems.

Acknowledgments

This research was supported by the U.S. Department of Energy (DOE), Office of Biological and Environmental Research (BER), as part of BER's Subsurface Biogeochemistry Research (SBR) Program. This contribution originates from the SBR Scientific Focus Area (SFA) at Pacific Northwest National Laboratory (PNNL). This research used resources of the National Energy Research Scientific Computing Center, a DOE Office of Science User Facility supported by the DOE's Office of Science under Contract No. DE-AC02-05CH11231. Requests for data not explicitly provided in the manuscript may be made to the corresponding author. PNNL is operated by Battelle for the DOE under Contract DE-AC05-76RL01830.

References

Anderson, B., Anderson, C., Christense, D., Inman, R., & Marti, J. (2016), *2015 Drought Response: Summary Report* (Rep. 16-11-001). Olympia, WA: Washington State Department of Ecology.

Arntzen, E. V., Geist, D. R., & Dresel, P. E. (2006), Effects of fluctuating river flow on groundwater/surface water mixing in the hyporheic zone of a regulated, large cobble bed river. *River Research and Applications*, 22(8), 937-946. doi: 10.1002/rra.947

Arrigoni, A. S., Poole, G. C., Mertes, L. A. K., O'Daniel, S. J., Woessner, W. W., & Thomas, S. A. (2008), Buffered, lagged, or cooled? Disentangling hyporheic influences on temperature cycles in stream channels. *Water Resources Research*, 44(9), W09418. doi: 10.1029/2007WR006480

Battin, T. J., Kaplan, L. A., Findlay, S., Hopkinson, C. S., Marti, E., Packman, A. I., Newbold, J. D., & Sabater, F. (2008), Biophysical controls on organic carbon fluxes in fluvial networks. *Nature Geoscience*, 1(2), 95-100. doi:10.1038/ngeo101

Baxter, C. V., Fausch, K. D., & Saunders, W. C. (2005), Tangled webs: Reciprocal flows of invertebrate prey link streams and riparian zones. *Freshwater Biology*, 50(2), 201-220. doi: 10.1111/j.1365-2427.2004.01328.x

Bjornstad, B. N., Lanigan, D. C, Horner, J. A., Thorne, P. D., & Vermeul, V. R. (2009), *Borehole completion and conceptual hydrogeologic model for the IFRC well field, 300 Area, Hanford Site* (Rep. PNNL-18340). Richland, WA: Pacific Northwest National Laboratory. doi: 10.2172/974984

Boano, F., Harvey, J. W., Marion, A., Packman, A. I., Revelli, R., Ridolfi, L., & Wörman, A. (2014), Hyporheic flow and transport processes: Mechanisms, models, and biogeochemical implications. *Reviews of Geophysics*, 52(4), 603-679. doi: 10.1002/2012RG000417

Boulton, A. J., Findlay, S., Marmonier, P., Stanley, E. H., & Valett, H. M. (1998), The functional significance of the hyporheic zone in streams and rivers. *Annual Review of Ecology, Evolution, and Systematics*, 29(1), 59-81.doi: 10.1590/1519-6984.15413

Briody, A. C., Cardenas, M. B., Shuai, P., Knappett, P. S. K., & Bennett, P. C. (2016), Groundwater flow, nutrient, and stable isotope dynamics in the parafluvial-hyporheic zone of the regulated Lower Colorado River (Texas, USA) over the course of a small flood. *Hydrogeology Journal*, 24(4), 923-935. doi: 10.1007/s10040-016-1365-3

Brunke, M., & Gonser, T. O. M. (1997), The ecological significance of exchange processes between rivers and groundwater. *Freshwater Biology*, 37(1), 1-33. doi: 10.1046/j.1365-2427.1997.00143.x

Buffington, J. M., & Tonina D. (2009), Hyporheic exchange in mountain rivers II: Effects of channel morphology on mechanics, scales, and rates of exchange. *Geography Compass*, 3(3), 1038-1062. doi: 10.1111/j.1749-8198.2009.00225.x

Burkholder, B. K., Grant G. E., Haggerty R., Khangaonkar T., & Wampler P. J. (2008), Influence of hyporheic flow and geomorphology on temperature of a large, gravel-bed river, Clackamas River, Oregon, USA. *Hydrological Processes*, 22(7), 941-953. doi: 10.1002/hyp.6984

Caissie, D. (2006), The thermal regime of rivers: A review, *Freshwater Biology*, **51**(8), 1389-1406. doi: 10.1111/j.1365-2427.2006.01597.x

Cardenas, M. B. (2015), Hyporheic zone hydrologic science: A historical account of its emergence and a prospectus. *Water Resources Research*, 51(5), 3601-3616. doi: 10.1002/2015WR017028

Cardenas, M. B., & Wilson, J. L. (2007), Dunes, turbulent eddies, and interfacial exchange with permeable sediments. *Water Resources Research*, 43(8), W08412. doi: 10.1029/2006WR005787

Cardenas, M. B., Wilson, J. L., & Zlotnik, V. A. (2004), Impact of heterogeneity, bed forms, and stream curvature on subchannel hyporheic exchange. *Water Resources Research*, 40(8), W08307. doi: 10.1029/2004WR003008

Casas-Mulet, R., Alfredsen, K., Brabrand, Å., & Saltveit, S. J. (2016), Hydropower operations in groundwater-influenced rivers: Implications for Atlantic salmon, Salmo salar, early life stage development and survival. *Fisheries Management and Ecology*, 23(2), 144-151. doi: 10.1111/fme.12165

Chen, X., Murakami, H., Hahn, M. S., Hammond, G. E., Rockhold, M. L., Zachara, J.M., & Rubin, Y. (2012), Three-dimensional Bayesian geostatistical aquifer characterization at the Hanford 300 area using tracer test data. *Water Resources Research*, 48, W06501. doi: 10.1029/2011WR010675.

Chen, X., Hammond, G. E., Murray, C. J., Rockhold, M. L., Vermeu, V. R., & Zachara, J. M. (2013), Application of ensemble-based data assimilation techniques for aquifer characterization using tracer data at Hanford 300 area. *Water Resources Research*, 49(10), 7064-7076. doi: 10.1002/2012WR013285

Conant, B., Cherry, J. A., & Gillham, R. W. (2004), A PCE groundwater plume discharging to a river: Influence of the streambed and near-river zone on contaminant distributions. *Journal of Contaminant Hydrology*, 73(1), 249-279. doi: 10.1016/j.jconhyd.2004.04.001

Constantz, J. (2008), Heat as a tracer to determine streambed water exchanges. *Water Resources Research*, 44(4), W00D10. doi: 10.1029/2008WR006996

Duncan, J. P., Burk, K. W., Chamness, M. A., Fowler, R. A., Fritz, B. G., Hendrickson, P. L.,. Kennedy, E. P, Last, G. V., Poston, T. M., & Sackschewsky, M. R. (2007), *Hanford Site National Environmental Policy Act (NEPA) characterization* (Rep. PNNL-6415 Rev.18). Richland, WA: Pacific Northwest National Laboratory.

Ebersole, J. L., Liss, W. J., & Frissell, C. A. (2003), Thermal heterogeneity, stream channel morphology, and salmonid abundance in northeastern Oregon streams. *Canadian Journal of Fisheries and Aquatic Sciences*, 60(10), 1266-1280. doi: 10.1139/f03-107

Farge, M. (1992), Wavelet transforms and their applications to turbulence. *Annual Review of Fluid Mechanics*, 24, 395–457. doi: 10.1146/annurev.fl.24.010192.002143

Francis, B. A., Francis, L. K., & Cardenas, M. B. (2010), Water table dynamics and groundwater-surface water interaction during filling and draining of a large fluvial island due to dam-induced river stage fluctuations. *Water Resources Research*, 46(7), W07513. doi: 10.1029/2009WR008694

Fritz, B. G., & Arntzen E. V. (2007), Effect of rapidly changing river stage on uranium flux through the hyporheic zone. *Ground Water*, 45(6), 753-760. doi: 10.1111/j.1745-6584.2007.00365.x

Galbraith, H. S., Blakeslee, C. J., & Lellis, W. A. (2012), Recent thermal history influences thermal tolerance in freshwater mussel species (Bivalvia: Unionoida). *Freshwater Science*, 31(1), 83-92. doi: 10.1899/11-025.1

Geist, D. R., Hanrahan, T. P., Arntzen, E. V., McMichael, G. A., Murray, C. J., & Chien, Y.-J. (2002), Physicochemical characteristics of the hyporheic zone affect redd site selection by chum salmon and fall chinook salmon in the Columbia River. *North American Journal of Fisheries Management*, 22(4), 1077-1085. doi: 10.1577/1548-8675(2002)022<1077:PCOTHZ>2.0.CO;2

Gerecht, K. E., Cardenas, M. B., Guswa, A. J., Sawyer, A. H., Nowinski, J. D., & Swanson, T. E. (2011), Dynamics of hyporheic flow and heat transport across a bed-to-bank continuum in a large regulated river. *Water Resources Research*, 47(3), W03524. doi: 10.1029/2010WR009794

Graf, W. L. (1999), Dam nation: A geographic census of American dams and their large-scale hydrologic impacts. *Water Resources Research*, 35(4), 1305-1311. doi: 10.1029/1999WR900016

Graham, P. W., Andersen, M. S., McCabe, M. F., Ajami, H., Baker, A., & Acworth, I. (2015), To what extent do long-duration high-volume dam releases influence river–aquifer interactions? A case study in New South Wales, Australia. *Hydrogeology Journal*, 23(2), 319-334. doi: 10.1007/s10040-014-1212-3

Gu, C., Anderson, W., & Maggi, F. (2012), Riparian biogeochemical hot moments induced by stream fluctuations. *Water Resources Research*, 48(9), W09546. doi: 10.1029/2011WR011720

Gu, C., Hornberger, G. M., Mills, A. L., Herman, J. S., & Flewelling, S. A. (2007), Nitrate reduction in streambed sediments: Effects of flow and biogeochemical kinetics. *Water Resources Research*, 43(12), W12413. doi:10.1029/2007WR006027

Hammond, G. E., Lichtner, P. C., & Mills, R. T. (2014), Evaluating the performance of parallel subsurface simulators: An illustrative example with PFLOTRAN. *Water Resources Research*, 50(1), 208-228. doi: 10.1002/2012WR013483

Hanrahan, T. P. (2007), Large-scale spatial variability of riverbed temperature gradients in Snake River fall Chinook salmon spawning areas. *River Research and Applications*, 23(3), 323-341. doi: 10.1002/rra.982

Kompala, D. S., Ramkrishna, D., Jansen, N. B., & Tsao, G. T. (1986), Investigation of bacterial growth on mixed substrates: Experimental evaluation of cybernetic models. *Biotechnology and Bioengineering*, 28(7), 1044-1055. doi: 10.1002/bit.260280715

Kurylyk, B. L., MacQuarrie, K. T., Linnansaari, T., Cunjak, R. A., & Curry, R. A. (2015), Preserving, augmenting, and creating cold-water thermal refugia in rivers: Concepts derived from research on the Miramichi River, New Brunswick (Canada). *Ecohydrology*, 8(6), 1095-1108. doi: 10.1002/eco.1566

Lautz, L. K., & Fanelli, R. M. (2008), Seasonal biogeochemical hotspots in the streambed around restoration structures. *Biogeochemistry*, 91(1), 85-104. doi: 10.1007/s10533-008-9235-2

Li, M., Gao, Y., Qian, W.-J., Shi, L., Liu, Y., Nelson, W. C., Nicora, C. D., Resch, C. T., Thompson, C., Yan, S., Fredrickson, J. K., Zachara, J. M., & Liu, C. (2017) Targeted quantification of functional enzyme dynamics in environmental samples for microbially mediated biogeochemical processes. *Environmental Microbiology Reports*, 9(5), 512-521. doi: 10.1111/1758-2229.12558

Ma, R., Zheng, C., Zachara, J. M., & Tonkin, M. (2012), Utility of bromide and heat tracers for aquifer characterization affected by highly transient flow conditions. *Water Resources Research*, 48(8), W08523. doi: 10.1029/2011WR011281

McCallum, J. L., & Shanafield, M. (2016), Residence times of stream-groundwater exchanges due to transient stream stage fluctuations. *Water Resources Research*, 52(3), 2059-2073. doi: 10.1002/2015WR017441

McClain, M. E., Boyer, E. W., Dent, C. L., Gergel, S. E., Grimm, N. B., Groffman, P. M., … Pinay, G. (2003), Biogeochemical hot spots and hot moments at the interface of terrestrial and aquatic ecosystems. Ecosystems, 6(4), 301-312. doi: 10.1007/s10021-003-0161-9

Mejia, F. H., Baxter, C. V., Berntsen, E. K., & Fremier, A. K. (2016), Linking groundwater – surface water exchange to food production and salmonid growth. *Canadian Journal of Fisheries and Aquatic Sciences*, 73(11), 1650-1660. doi: 10.1139/cjfas-2015-0535

Nilsson, C., Reidy, C. A., Dynesius, M., & Revenga, C. (2005), Fragmentation and flow regulation of the world's large river systems. *Science*, 308(5720), 405-408. doi: 10.1126/science.1107887

Pebesma, E. J. (2004), Multivariable geostatistics in S: the gstat package. *Computers & Geosciences*, 30(7), 683-691. doi: 10.1016/j.cageo.2004.03.012

Ramkrishna, D., & Song H.-S. (2012), Dynamic models of metabolism: Review of the cybernetic approach. *AIChE Journal*, 58(4), 986-997. doi: 10.1002/aic.13734

Richardson, J. S., Zhang, Y., & Marczak, L. B. (2010), Resource subsidies across the land–freshwater interface and responses in recipient communities. *River Research and Applications,* 26(1), 55-66. doi: 10.1002/rra.1283

Rittmann, B. E., & McCarty P. L. (2001), *Environmental Biotechnology*: *Principles and Applications*. New York City, NY: McGraw-Hill.

Rockhold, M. L., Fayer, M. J., Kincaid, C. T., & Gee, G. W. (1995), *Estimation of natural groundwater recharge for the performance assessment of a low-level waste disposal facility at the Hanford Site* (Rep. PNL-10508). Richland, WA: Pacific Northwest National Laboratory.

Roesch, A., & Schmidbauer, H. (2015), *WaveletComp: Computational wavelet analysis, R Package Version, 1.0*. Retrieved from https://cran.r-project.org/web/packages/WaveletComp/WaveletComp.pdf.

Salehin, M., Packman, A. I., & Paradis, M. (2004), Hyporheic exchange with heterogeneous streambeds: Laboratory experiments and modeling. *Water Resources Research*, 40(11), W11504. doi: 10.1029/2003WR002567

Sawyer, A. H., Cardenas, M. B., Bomar, A., & Mackey, M. (2009), Impact of dam operations on hyporheic exchange in the riparian zone of a regulated river. *Hydrological Processes*, 23(15), 2129-2137. doi: 10.1002/hyp.7324

Schmadel, N. M., Ward, A. S., Lowry, C. S., & Malzone, J. M. (2016), Hyporheic exchange controlled by dynamic hydrologic boundary conditions. *Geophysical Research Letters*, 43(9), 4408-4417. doi: 10.1002/2016GL068286

Slater, L. D., Ntarlagiannis, D., Day-Lewis, F. D., Mwakanyamale, K., Versteeg, R. J., Ward, A., … Lane, J. W. (2010), Use of electrical imaging and distributed temperature sensing methods to characterize surface water-groundwater exchange regulating uranium transport at the Hanford 300 Area, Washington. *Water Resources Research*, 46(10), W00153. doi: 10.1029/2010WR009110

Song, H. S., & Liu, C. (2015), Dynamic metabolic modeling of denitrifying bacterial growth: the cybernetic approach. *Industrial & Engineering Chemistry Research*, 54(42), 10221-10227. doi: 10.1021/acs.iecr.5b01615

Song, H. S., Cannon, W. R., Beliaev, A. S., & Konopka, A. (2014), Mathematical modeling of microbial community dynamics: A methodological review. *Processes*, 2(4), 711-752. doi: 10.3390/pr2040711

Song, H. S., Thomas, D. G., Stegen, J. C., Li, M., Liu, C., Song, X., Chen, X., Fredrickson, J. K., Zachara, J. M., & Scheibe, T. D. (2017), Regulation-structured dynamic metabolic model provides a potential mechanism for delayed enzyme response in denitrification process. *Frontiers in Microbiology*, 8, 1866. doi: 10.3389/fmicb.2017.01866

Stegen, J. C., Fredrickson, J. K., Wilkins, M. J., Konopka, A. E., Nelson, W. C., Arntzen, E. V., Chrisler, W. B., Chu, R. K., Danczak, R. E., Fansler, S. J., Kennedy, D. W., Resch, C. T., & Tfaily, M. (2016), Groundwater-surface water mixing shifts ecological assembly processes and stimulates organic carbon turnover. *Nature Communications*, 7, 11237. doi: 10.1038/ncomms11237

Stonedahl, S. H., Harvey, J. W., & Packman, A. I. (2013), Interactions between hyporheic flow produced by stream meanders, bars, and dunes. *Water Resources Research*, 49(9), 5450-5461. doi: 10.1002/wrcr.20400

Trauth, N., Schmidt, C., Vieweg, M., Maier, U., & Fleckenstein, J. H (2014), Hyporheic transport and biogeochemical reactions in pool-riffle systems under varying ambient groundwater flow conditions. *Journal of Geophysical Research: Biogeosciences*, 119, 910-28. doi: 10.1002/2013JG002586

Trauth, N., & Fleckenstein, J. H. (2017), Single discharge events increase reactive efficiency of the hyporheic zone. *Water Resources Research*, 53(1), 779–798. doi: 10.1002/2016WR019488

Whitledge, G. W., Rabeni, C. F., Annis, G., & Sowa, S. P. (2006), Riparian shading and groundwater enhance growth potential for smallmouth bass in Ozark streams. *Ecological Applications*, 16(4), 1461-1473. doi: 10.1890/1051-0761(2006)016[1461:RSAGEG]2.0.CO;2

Williams, M., Thorne, P., Rockhold, M., & Chen, Y. (2008), *Three-dimensional groundwater models of the 300 Area at the Hanford Site, Washington State* (Rep. PNNL-17708). Richland, WA: Pacific Northwest National Laboratory.

Yan, S., Liu, Y., Liu, C., Shi, L., Shang, J., Shan, H., Zachara, J., Fredrickson, J., Kennedy, D., Resch C. T., Thompson C., Fansler, S. & Fansler, S. (2016), Nitrate bioreduction in redox-variable low permeability sediments. *Science of The Total Environment*, 539, 185-195. doi: 10.1016/j.scitotenv.2015.08.122

Ye, S., Covino, T. P., Sivapalan, M., Basu, N. B., Li, H. Y., & Wang, S. W. (2012), Dissolved nutrient retention dynamics in river networks: A modeling investigation of transient flows and scale effects. *Water Resources Research*, 48(6), W00J17. doi: 10.1029/2011WR010508

Yellen, B., & Boutt, D. F. (2015), Hydropeaking induces losses from a river reach: Observations at multiple spatial scales. *Hydrological Processes*, 29(15), 3261-3275. doi: 10.1002/hyp.10438

Young, J. D., & Ramkrishna, D. (2007), On the matching and proportional laws of cybernetic models. *Biotechnology Progress*, 23(1), 83-99. doi: 10.1021/bp060176q

Zachara, J. M., Chen, X. Y., Murray, C., & Hammond, G. E. (2016), River stage influences on uranium transport in a hydrologically dynamic groundwater-surface water transition zone. *Water Resources Research*, 52(3), 1568-1590. doi: 10.1002/2015WR018009

Zachara, J. M., Freshley, M. D., Last, G. V., Peterson, R. E., & Bjornstad, B. N. (2012), *Updated conceptual model for the 300 Area uranium groundwater plume* (Rep. PNNL-22048), Richland, WA: Pacific Northwest National Laboratory.

Zachara, J. M., Long, P. E., Bargar, J., Davis, J. A., Fox, P., Fredrickson, J. K., … Yabusaki, S. B. (2013), Persistence of uranium groundwater plumes: contrasting mechanisms at two DOE sites in the groundwater-river interaction zone. *Journal of Contaminant Hydrology,* 147, 45-72. doi: 10.1016/j.jconhyd.2013.02.001

LIST OF FIGURES

(a) Sketch of the river reach

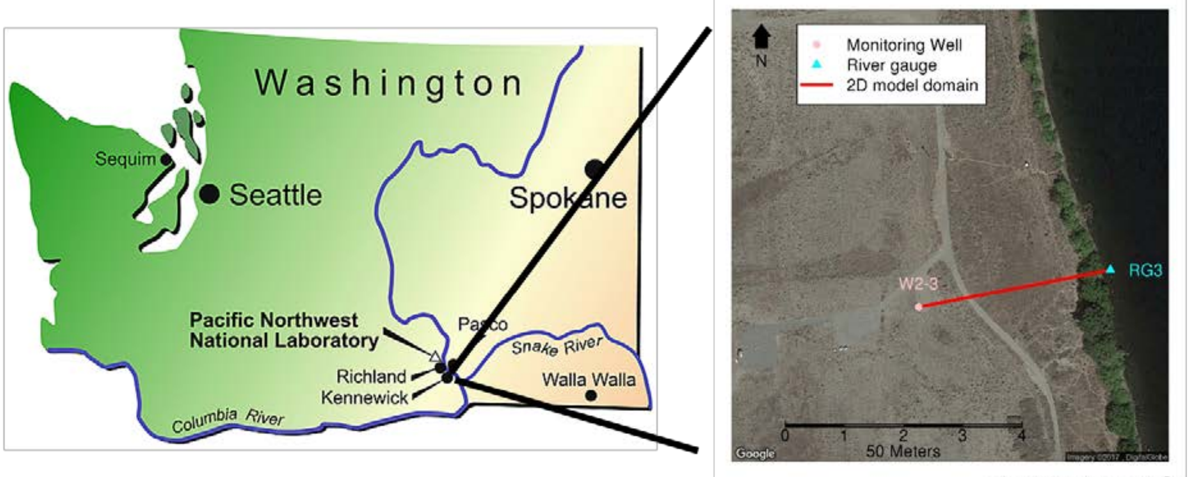

(b) Permeability field

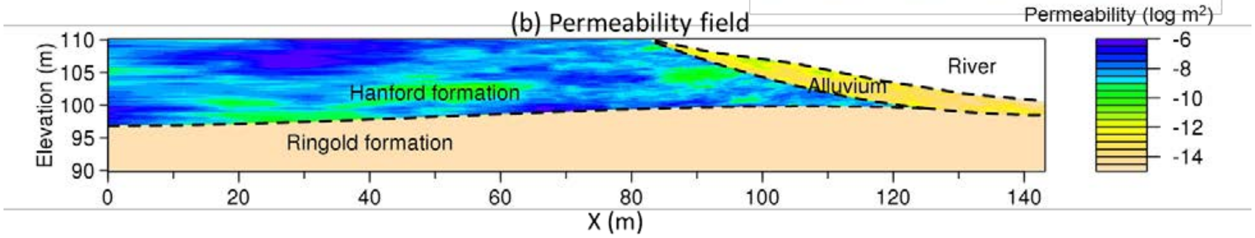

Figure 1. Location map and conceptual model. (a) Sketch of the river reach. W2-3 represents the inland groundwater monitoring well, and RG3 denotes the river gauge with contiunous level and temperature data. (b) Permeability field.

(a) Observed discharge and naturalized discharge of Priest Rapids Dam from RMJOC

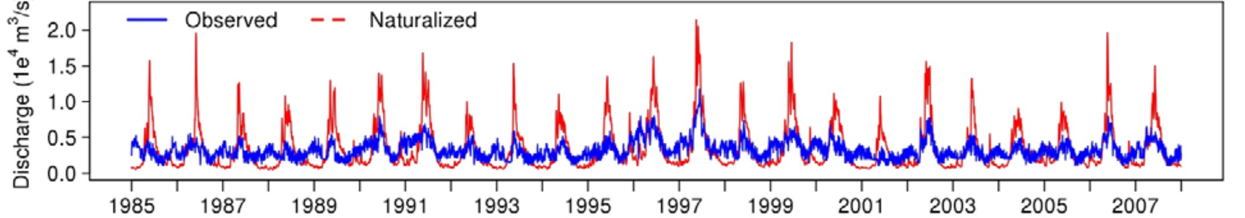

(b) Wavelet power spectrum of dam discharge

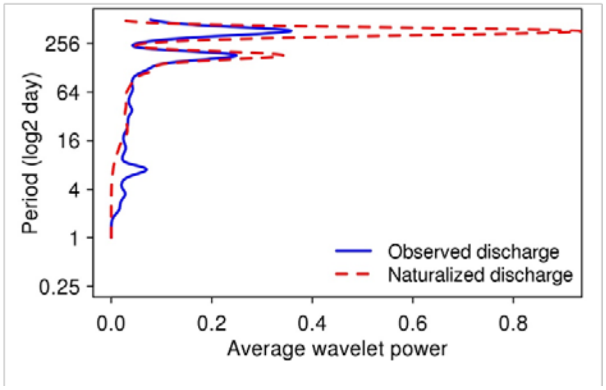

Figure 2. Dishcarge data anaysis results. (a) Historical daily discharge data (real observed and naturalized). (b) Average wavelet power spectrum of discharge (real observed and naturalized).

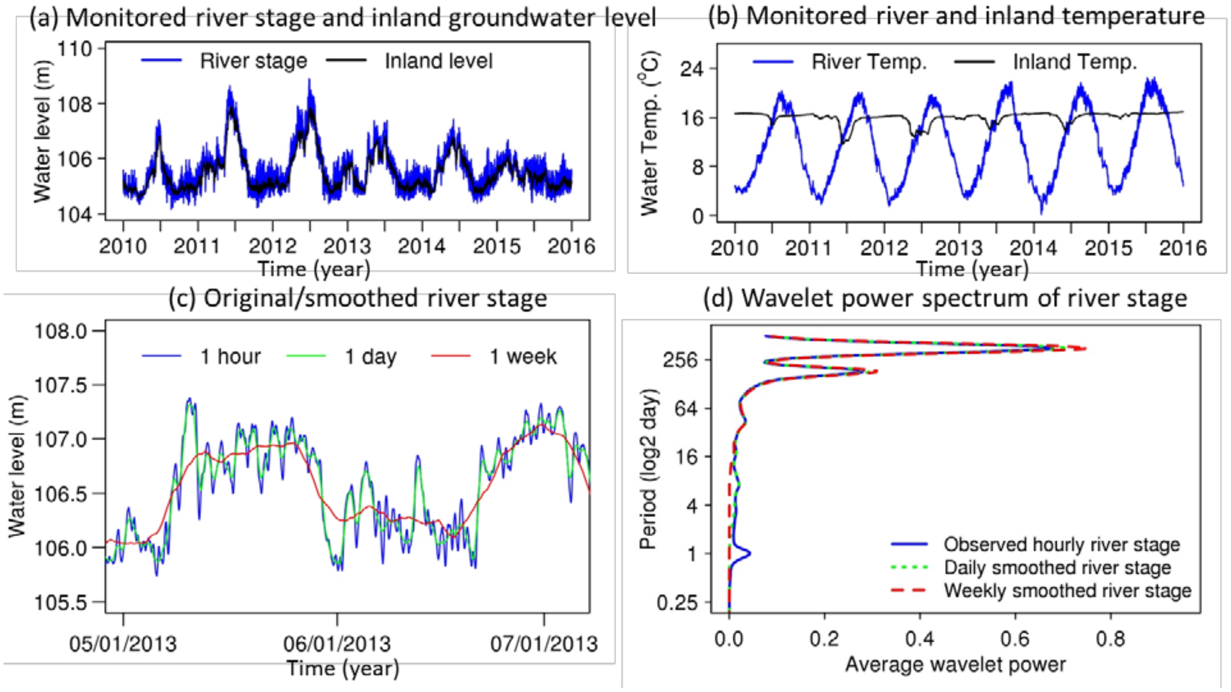

Figure 3. Boundary conditions. (a) Monitored hourly river stage and inland groundwater level. (b) Monitored hourly river temperature and inland groundwater temperature. (c) A segment of observed and smoothed river stage. (d) Average wavelet power spectrum of stage (real observed and smoothed).

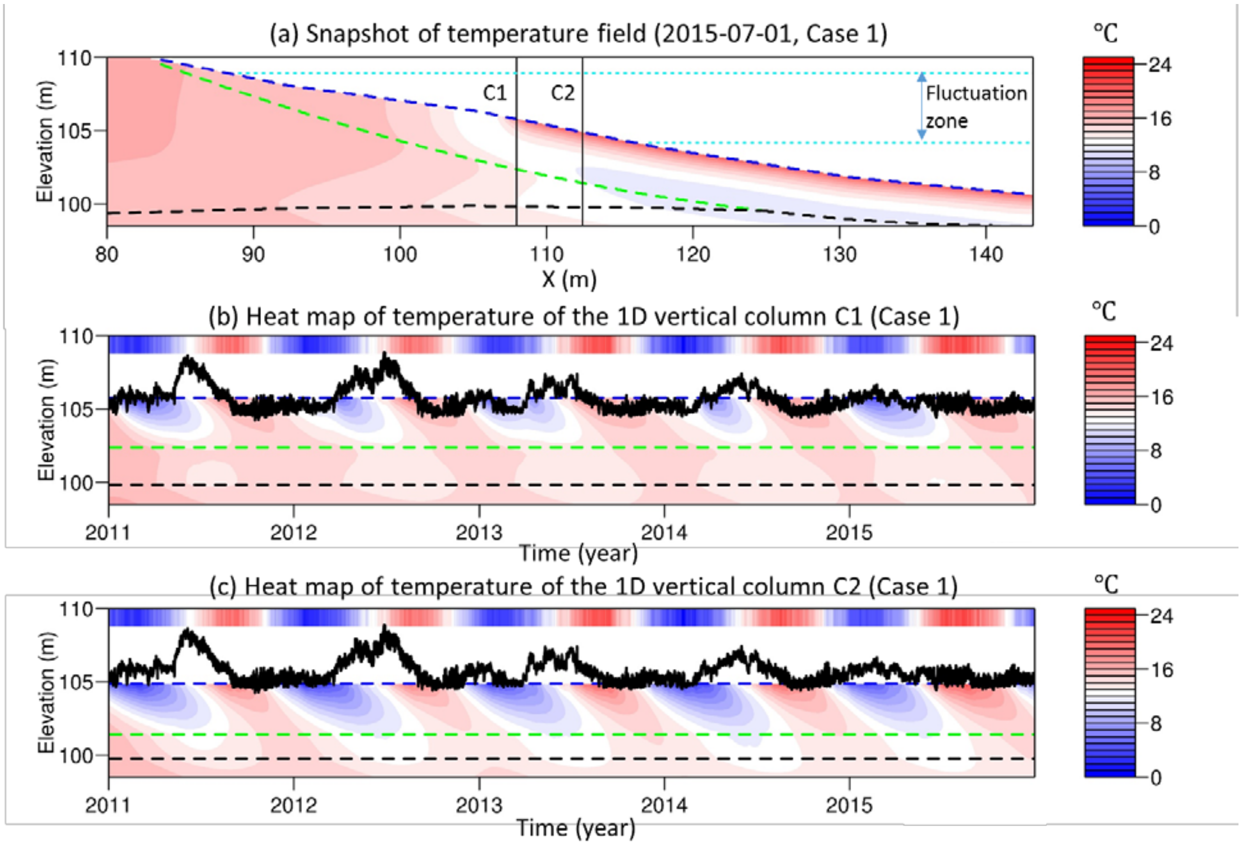

Figure 4. Temperature simulation results. (a) Snapshot of the temperature field (Case 1, the case with original hydrologic boundary conditions), zoomed in to focus on the alluvium and near-shore Hanford. The colored dash lines are the formation boundaries. The snapshot was taken on 2015-07-01 00:00 to illustrate the cold-water zone in summer. (b-c) Temperature time series of representative vertical columns (the vertical lines in panel (a) of Case 1) illustrate temperature lags in the HZ. The top crossband shows the temperature of river water, and the bottom contour shows the temperature dynamics along the 1D column. The black curve represents the river stage over the five-year window, and the colored dashed lines are the formation boundaries corresponding to those in panel (a).

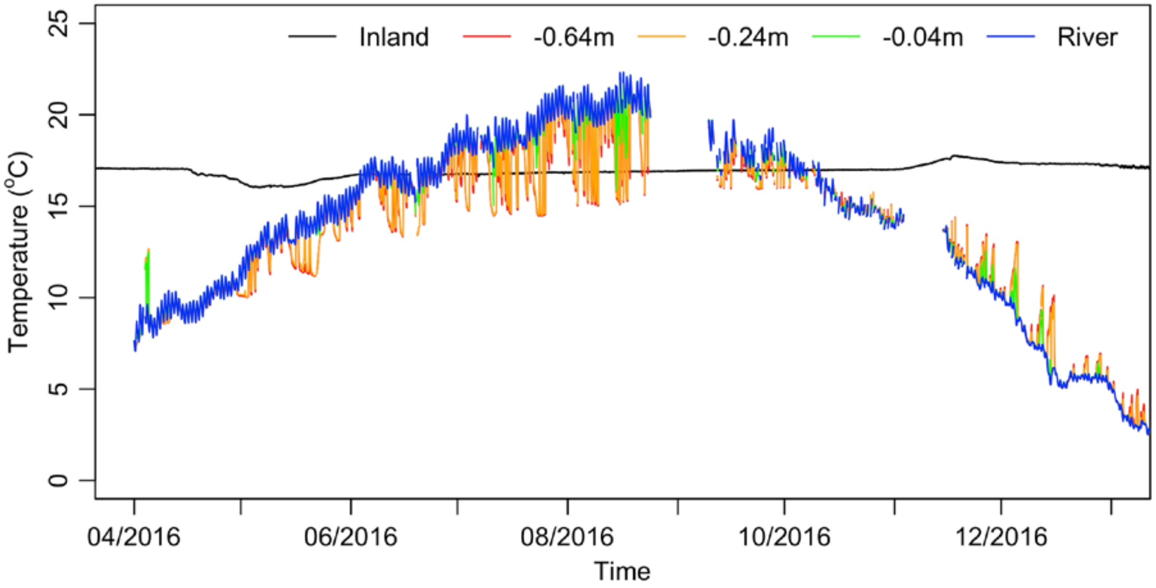

Figure 5. *In situ* measurements from a multi-depth thermistor array.

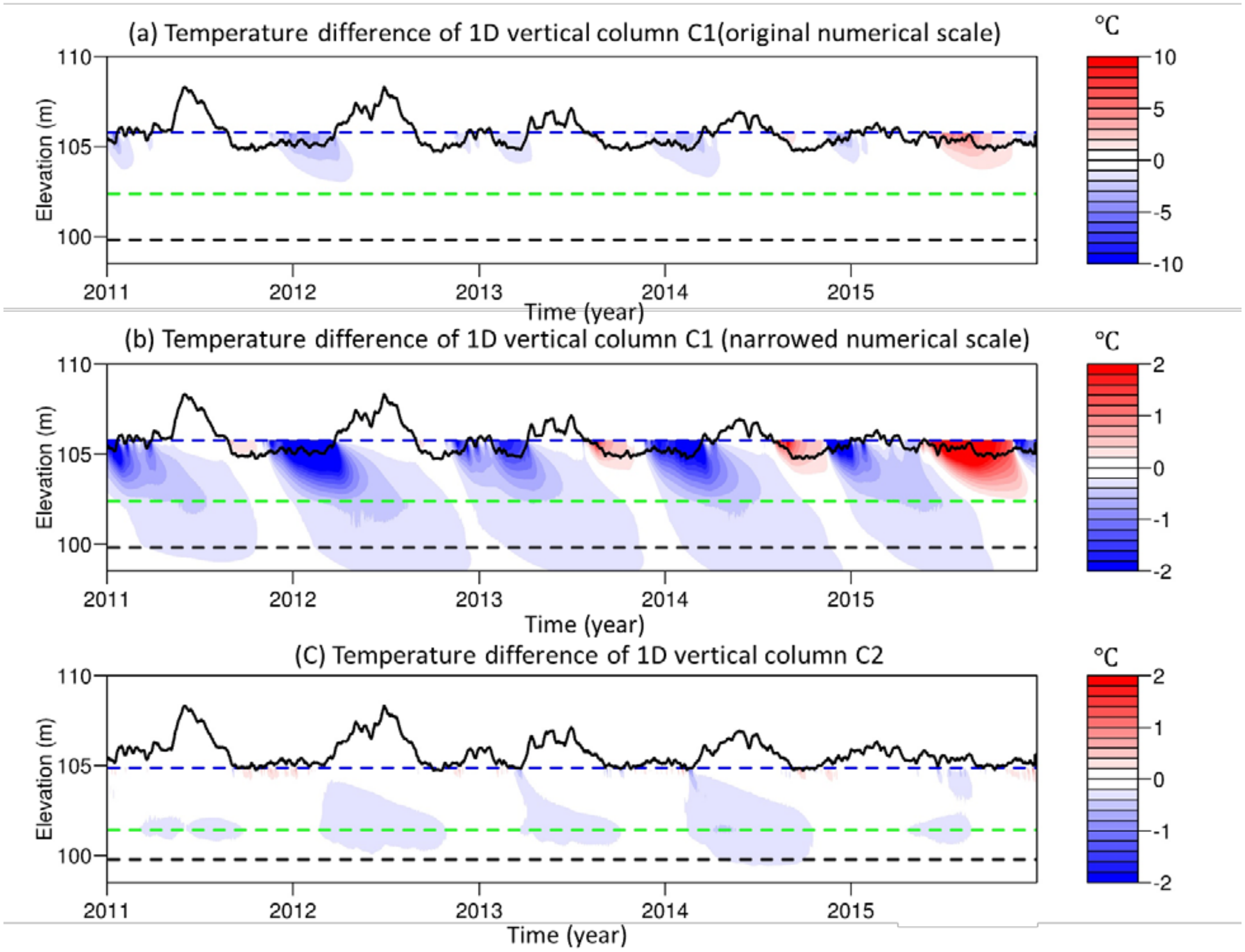

Figure 6. Temperature difference of the 1D column between cases (Case 1 minus Case 2. Case 1 has original boundary. Case 2 uses weekly smoothed hydrologic boundary). The temperature diffference range is between -10ºC and 5ºC. The color scheme is chosen to show positive differences in red, negative differences in blue, and white color for no differences. Both panels (a) and (b) are the temperature difference of the column C1 in Figure 4(a) with panel (a) showing the differences in full range, while panel (b) caps the differences at ±2ºC for finer resolutions. (c) Temperature difference of column C2 in Figure 4(a).

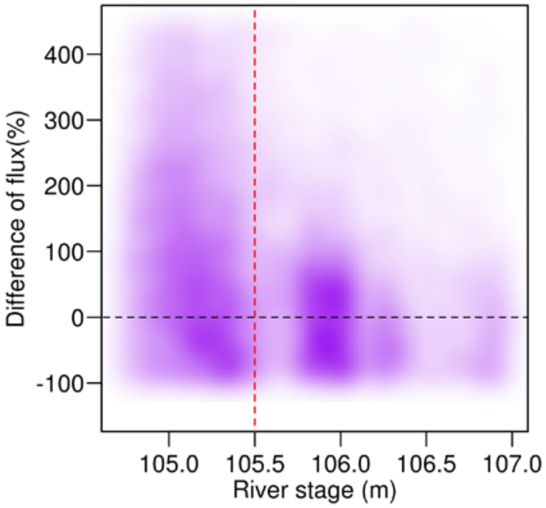

Figure 7. Percentage difference of flux across the riverbed $\left[(F_1 - F_2)/F_2 * 100\%\right]$ versus river stage. F_1 is the exchange flux of the case with hourly hydrologic boundary, and F_2 is the exchange flux of the case with weekly smoothed hydrologic. The black dashed line marks where the difference was zero. The red dashed line was at average river stage during the five-year simulation (105.5 m). This scatter density plot shows both the location and density of data points, and the darker color means more data points.

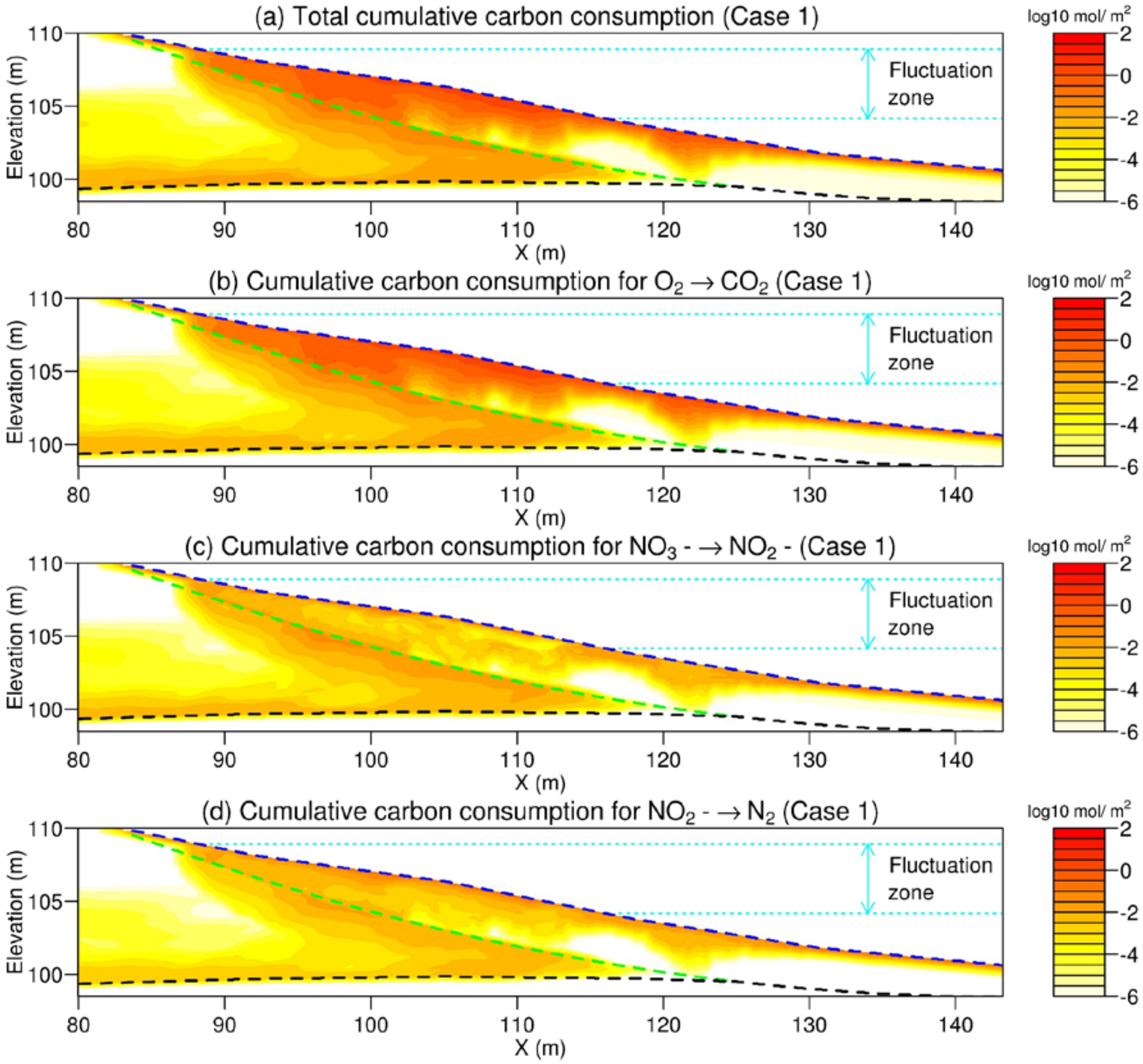

Figure 8. Spatial distribution of cumulative carbon consumption in Case 1, the case with hourly hydrologic boundary (log10, mol/m^2). (a) Total cumulative carbon consumption. (b) The cumulative carbon consumption for O_2 → CO_2. (c) The cumulative carbon consumption for NO_3^- → NO_2-. (d) The cumulative carbon consumption for NO_2- → N_2.

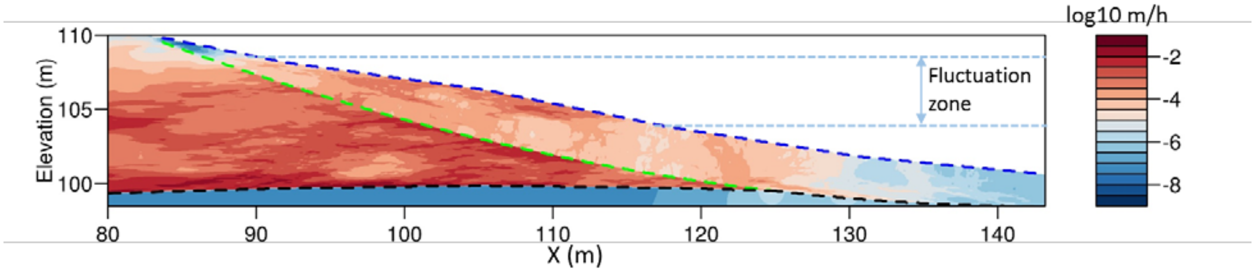

Figure 9. Mean Darcy velocity field during five-year simulation (log10 m/h) of Case 1, the case with hourly hydrologic boundary.

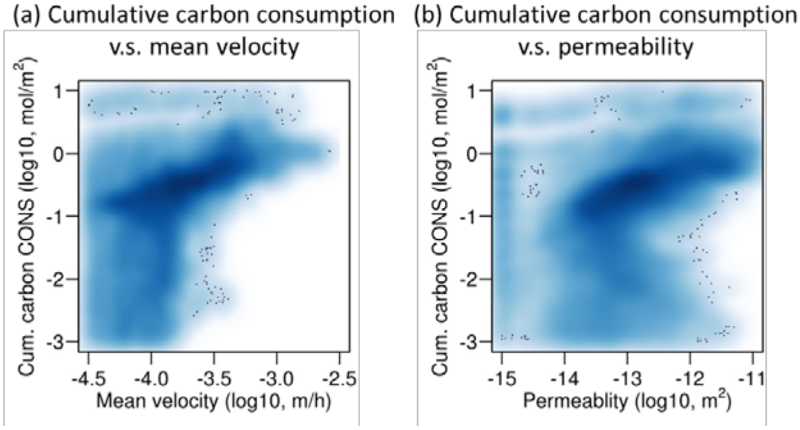

(a) Cumulative carbon consumption v.s. mean velocity

(b) Cumulative carbon consumption v.s. permeability

Figure 10. Relation between cell-based cumulative carbon consumption and mean velocity (a) and permeability (b) in alluvium during the five-year simulation period for Case 1, the case with hourly hydrologic boundary. These scatter density plots show both the location and density of data points, and the darker color means more data points. Similar patterns hold for all other cases.

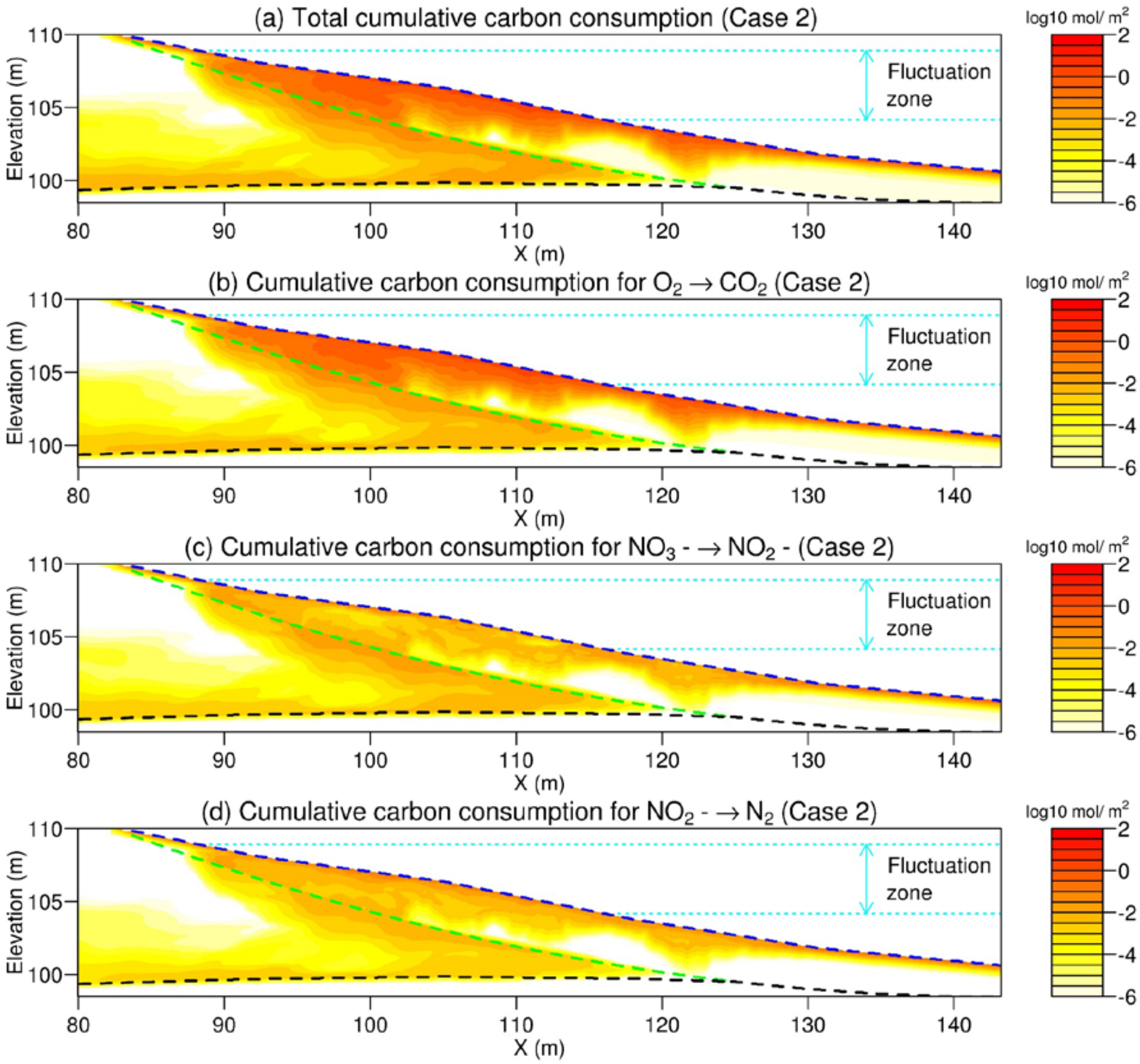

Figure 11. Spatial distribution of cumulative carbon consumption in Case 2, the case with weekly smoothed hydrologic boundary (log10, mol/m^2). (a) Total cumulative carbon consumption. (b) The cumulative carbon consumption for $O_2 \rightarrow CO_2$. (c) The cumulative carbon consumption for $NO_3^- \rightarrow NO_2$-. (d) The cumulative carbon consumption for NO_2- → N_2.

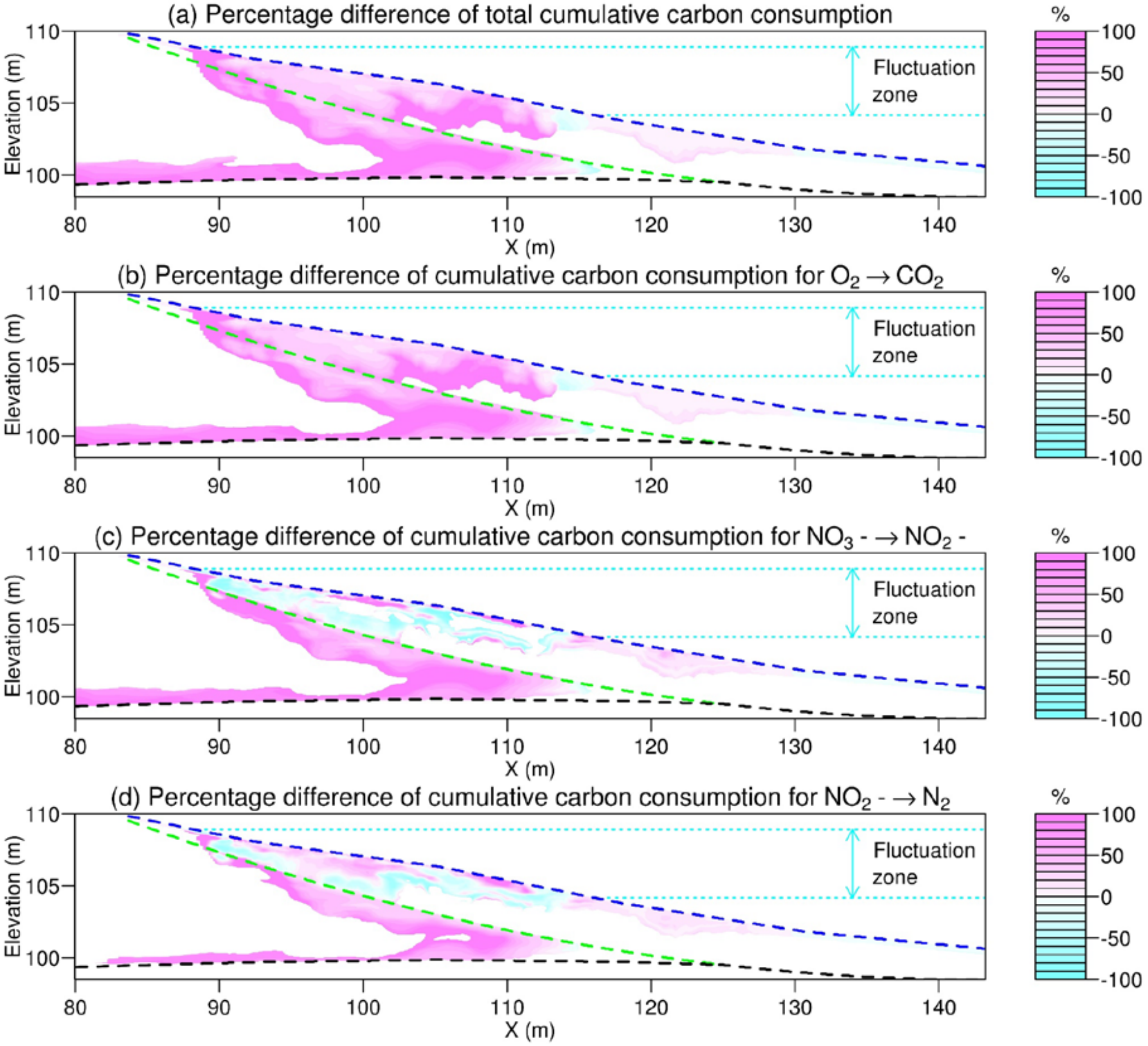

Figure 12. Spatial distribution of percentage difference of cumulative carbon consumption $\left[(C_{i,1}-C_{i,2})/C_{i,2}*100\%\right]$. $C_{i,1}$ is the cumulative carbon consumption in the case with hourly hydrologic boundary, and $C_{i,2}$ is the cumulative carbon consumption in the case with weekly smoothed hydrologic boundary. (a) Percentage difference of total cumulative carbon consumption. (b) Percentage difference of the cumulative carbon consumption for $O_2 \rightarrow CO_2$. (c) Percentage difference of the cumulative carbon consumption for $NO_3^- \rightarrow NO_2$-. (d) Percentage difference of the cumulative carbon consumption for NO_2- → N_2. The area with very low accumulative carbon consumption (i.e, 1×10^{-3} mol/m^2) was removed from this contour.

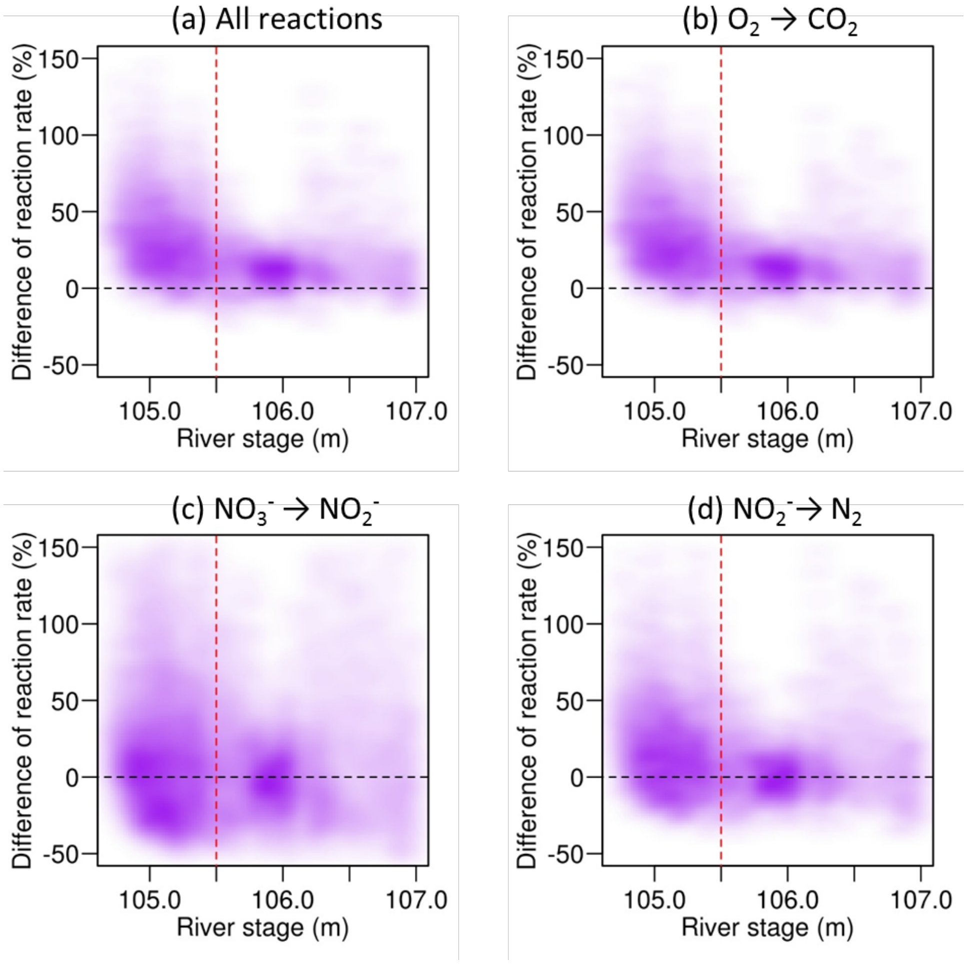

Figure 13. Percentage difference of the carbon consumption rate in alluvium $\left[(r_{i,1}-r_{i,2})/r_{i,2}*100\%\right]$ versus river stage. $r_{i,1}$ is the carbon consumption rate in the case with hourly hydrologic boundary, and $r_{i,2}$ is the carbon consumption rate in the case with weekly smoothed hydrologic boundary. (a) Percentage difference of total carbon consumption rate versus river stage. (b) Percentage difference of the carbon consumption rate for O_2 → CO_2 versus river stage. (c) Percentage difference of the carbon consumption rate for NO_3^- → NO_2- versus river stage. (d) Percentage difference of the carbon consumption rate for NO_2- → N_2 versus river stage. The black dashed line mark where the difference was zero. The red dashed line was at average river stage during the five-year simulation (105.5 m). These scatter density plots show both the location and density of data points, and the darker color means more data points.

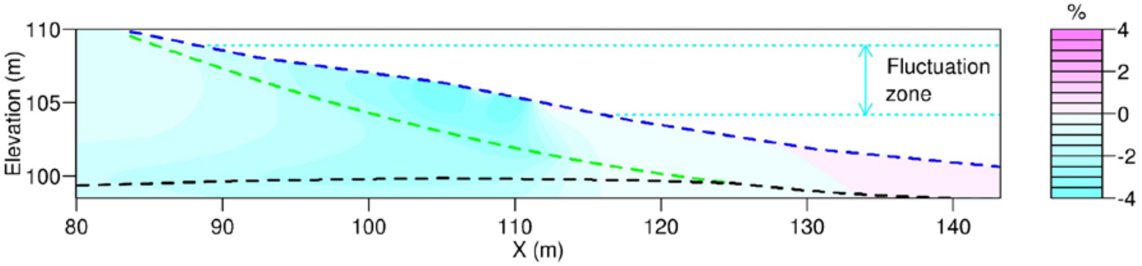

Figure 14. Time-averaged percentage difference of carbon consumption rate induced by altered temperature between the case with hourly hydrologic boundary (Case 1) and weekly smoothed hydrologic boundary (Case 2)

LIST OF TABLES

Table 1. Hydraulic and thermal properties of Hanford/alluvium/Ringold in the 2D model

	Hanford	**Alluvium**	**Ringold**
Geostatistical parameters of permeability field (exponential variogram**)**			
Mean (log, m^2)	-8.13	-13	-15
SD (log, m^2)	0.83	0.81	homogenous
Integral scale (m)	20	8	homogenous
Anisotropy ratio	0.1	0.1	homogenous
Anisotropy angle (◦)	-3	9	homogenous
Nugget	0	0	homogenous
Other hydraulic properties			
Porosity (-)	0.2	0.43	0.43
Residual saturation (-)	0.16	0.13	0.13
van Genuchten alpha parameter (Pa^{-1})	7.27e-4	1.43e-4	1.43e-4
van Genuchten m parameter [-]	0.34	0.75	0.75
Thermal properties			
Soil particle density of material (kg/m^3)	2760	2650	2650
Specific heat capacity of material (J/kg·K)	715	920	920
Wet thermal conductivity of material (W/K·m)	1.88	0.93	0.93
Dry thermal conductivity of material (W/K·m)	0.93	0.68	0.68

Table 2. Biogeochemical reaction parameters

Parameter	**$NO_3^- \rightarrow NO_2^-$**	**$NO_2^- \rightarrow N_2$**	**$O_2 \rightarrow CO_2$**
f_i [-]	$f_1 = 0.65$	$f_2 = 0.99$	$f_3 = 1/3\ f_1$
K_i [mmol/mmol BM/d]	$K_1 = 28.26$	$K_2 = 23.28$	$K_3 = 3\ K_1$
$K_{d,i}$[mM]	$K_{d,1} = 0.25$	$K_{d,2} = 0.25$	$K_{d,3} = K_{d,1}$
$K_{a,i}$[mM]	$K_{a,1} = 0.001$	$K_{a,2} = 0.004$	$K_{a,3} = K_{a,1}$
k_{deg} [mmol/mmol BM/d]	0.242		

Table 3. Solute concentration on boundaries

Solute	**Groundwater [mmol/L]**	**River [mmol/L]**
CH_2O	4.16×10^{-2}	2.58×10^{-1}
CO_2	2.48	1.12
NO_3^-	3.96×10^{-1}	8.87×10^{-3}
O_2	2.67×10^{-1}	3.59×10^{-1}
$C_5H_7O_2N$	1.00×10^{-2}	1.00×10^{-2}
N_2	1×10^{-7}	1×10^{-7}
NH_4+	1×10^{-7}	1×10^{-7}
NO_2-	1×10^{-7}	1×10^{-7}